PHYSICAL REVIEW MATERIALS **6**, 053604 (2022)

First-principles computational tensile test of γ-Fe grain boundaries considering the effect of magnetism: Electronic origin of grain boundary embrittlement due to Zn segregation

Kazuma Ito,[*] Yuta Tanaka, Takuya Mitsunobu, Takahiko Kohtake, Kazumasa Tsutsui, and Hideaki Sawada
Advanced Technology Research Laboratories, Nippon Steel Corporation, 20–1 Shintomi, Futtsu-city, Chiba 293–8511, Japan

(Received 31 January 2022; revised 22 March 2022; accepted 11 April 2022; published 9 May 2022)

The development of high-strength steels requires detailed understanding of the effect of solute elements on γ-Fe grain boundaries (GBs). In this study, first-principles computational tensile tests (FPCTT) were conducted on γ-Fe GBs to elucidate the mechanism of GB embrittlement due to Zn segregation. The paramagnetic γ-Fe GB was simulated by the $\Sigma5$ (310) GB in the antiferromagnetic double-layer (AFMD) configuration. The FPCTTs revealed that the fracture stress and fracture energy of the γ-Fe GB were reduced by Zn segregation, which is consistent with experimental results. Crystal orbital Hamilton population analysis was also performed to investigate the change in electronic states during the tensile process, and the enhancement of GB fracture by Zn segregation is caused by the breaking of the covalent-like bonds between Fe and Zn at a relatively small strain compared to the Fe–Fe bonds. This behavior is attributed to the localized nature of the $3d$ orbitals of Zn in γ-Fe. The FPCTTs of γ-Fe GBs using the AFMD properly consider the effect of magnetism in paramagnetic γ-Fe under tensile strain and is useful for investigating the effects of various solute elements on GB fracture and for the development of high-strength steels.

DOI: 10.1103/PhysRevMaterials.6.053604

I. INTRODUCTION

Grain boundary (GB) segregation affects various properties of polycrystalline metallic materials. GB embrittlement is well known in steel materials, in which mechanical properties and manufacturability are significantly degraded when certain solute elements segregate at GBs [1–5]. In recent years, the demand for high-strength steels has been increasing, especially for automotive applications, owing to CO_2 emission regulations and crash safety, and research and development of such steels has been conducted [6–11]. However, since the susceptibility to GB embrittlement increases with increasing material strength [12], GB embrittlement has emerged as an important issue in the development of high-strength steels.

To address this concern, many studies have been conducted on GB segregation and GB embrittlement in α-Fe (low-temperature bcc phase), which also shows the effectiveness of first-principles calculations and analyses using interatomic potentials. For instance, first-principles computational tensile tests (FPCTTs) on the tilt GBs can semiquantitatively reproduce the effects of various solute elements on the GB embrittlement or strengthening in α-Fe polycrystals [13–17]. First-principles calculations have also been useful for investigating the GB segregation tendency of solute elements and the electronic origin of this phenomenon [15,18–24]. More recently, GB segregation has also been analyzed using high-precision interatomic potentials based on first-principles calculations [25,26]. Furthermore, the amount of GB segregation of solute elements can be accurately predicted by calculations using a GB model that simulates polycrystals [27–30].

On the other hand, recent experimental studies have shown the importance of understanding the GB segregation tendency and the GB strengthening/embrittlement effect of solute elements in γ-Fe (high-temperature fcc phase). In high-strength martensitic steels, the segregation of solute elements at γ-Fe GBs during heat treatment has a significant effect on the GB embrittlement owing to hydrogen segregation at the GBs [10,31,32]. In addition, cracking along GBs during the welding of Zn-coated steels has been identified as a problem and has been the subject of recent research [33–36]. It was suggested that the crack initiation was caused by the embrittlement of the γ-Fe GB by Zn [35]. Furthermore, Zn causes cracking at the γ/α interphase boundaries at high temperature [37]. Thus, the solute element segregation, as well its strengthening and embrittlement effects at the γ-Fe and α-Fe GBs and at the γ/α interface boundaries, must be investigated.

However, because γ-Fe is generally paramagnetic in the temperature range where GB segregation occurs, and because of the difficulty in handling the magnetism, there have been only a few studies on GB segregation and GB embrittlement in γ-Fe using first-principles calculations. In fact, GB embrittlement by Zn has revealed that fractures occurred at γ-Fe GBs [33–35]. Furthermore, FPCTTs have been performed using α-Fe GBs instead [17,38] owing to the difficulty in handling the magnetism of γ-Fe. The effect of Zn and other alloying elements on the cohesive energy of the α/γ interface boundaries was also recently investigated by first-principles calculations [39], but γ-Fe without solute elements was treated as a ferromagnetic substance. Since the difference in the magnetic state of the matrix metal affects the GB embrittlement effect of the solute elements [40], magnetism should be considered in the FPCTTs conducted using γ-Fe GBs.

---

[*] ito.nn3.kazuma@jp.nipponsteel.com

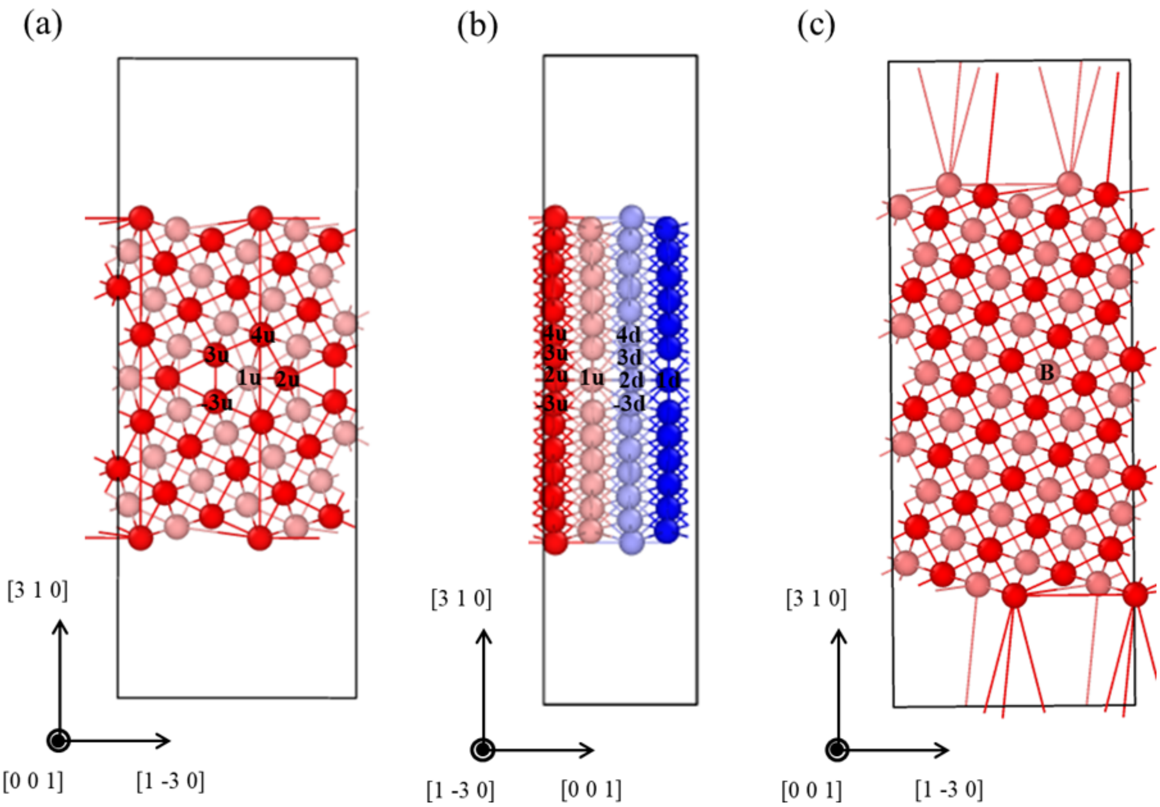

FIG. 1. Σ5(310) GB model from (a) [001] and (b) $[1\bar{3}0]$ axial directions. (c) Bulk model viewed along the [001] axis. The colors indicate the size of the coordinates along the [001] axis, and the numbers 1–4 are the indices of the equivalent GB sites. The red and pink atoms with the index u have positive magnetic moments, and the blue and light blue atoms with the index d have negative magnetic moments. B in the bulk model represents a site substituted for Zn.

In line with this, we show that the GB segregation of solute elements in paramagnetic γ-Fe can be well reproduced by first-principles calculations [41] by approximating paramagnetism with the antiferromagnetic double layer (AFMD) [42–45]. In this study, we perform and validate the FPCTT of γ-Fe GBs considering magnetism using the AFMD. Specifically, FPCTTs are performed on γ-Fe GBs (clean GB) and γ-Fe GBs with Zn segregation (GB with Zn) to evaluate the modeling of the GB embrittlement caused by Zn segregation. In addition, we investigate the electronic origin of the GB embrittlement, and show that it facilitates the electronic interpretation of the effect of solute elements on GB fracture. Crystal orbital Hamiltonian population (COHP) analysis [46–49] is applied to perform the electronic interpretation of the GB embrittlement, which allows us to establish a correlation between the energy change during the first-principles test process and the electronic state in terms of the band-structure energy change originating from the atomic-orbital pairs. Finally, from the perspective of magnetism treatment, we discuss the validity of the AFMD for FPCTTs on paramagnetic γ-Fe GBs.

II. COMPUTATIONAL METHOD

We simulated the magnetic state of the paramagnetic bulk γ-Fe and GBs using the AFMD state. The AFMD state is reportedly the most stable collinear state in γ-Fe with an fcc crystal structure [44]. The lattice constants and elastic properties of AFMD γ-Fe with cubic symmetry and varying interlayer distances in the [001] direction, in particular, are comparable to those of paramagnetic γ-Fe [42,50,51]. Therefore, we modeled the bulk and GBs of paramagnetic γ-Fe using the AFMD γ-Fe that exhibits a cubic symmetry. Hereafter, the AFMD γ-Fe with cubic symmetry will be simply referred to as the AFMD γ-Fe. The spin-polarized electronic structure calculations and structural optimization were performed using the Vienna *Ab initio* Simulation Package (VASP) with projector-augmented wave potentials [52,53]. The exchange-correlation effects were treated within the framework of the generalized gradient approximation (GGA) using the Perdew-Burke-Ernzerhof parametrization [54]. The cutoff energy for the plane-wave basis set was 350 eV. The Brillouin-zone integration was sampled using a k spacing of 0.3 Å^{-1} based on the Monkhorst-Pack scheme [55], and the Methfessel-Paxton smearing method [56] was used with a width of 0.2 eV. Under these conditions, the lattice constant and magnetic moment of the AFMD γ-Fe obtained are 3.54 Å and 1.93 μ_B, respectively [42,50,51]. Moreover, in this AFMD γ-Fe, the interlayer distance between the layers with the same magnetic moment and layers with different magnetic moments is 1.84 and 1.70 Å, respectively. All of these findings are consistent with previous studies [50,51].

The GB model shown in Fig. 1 includes a Σ5(310) GB and two (310) surfaces. The GB model was constructed using the

AFMD γ-Fe unit cell and includes 27 atomic layers and a 15-Å vacuum layer in the [310] direction. This vacuum layer is sufficiently thick to eliminate surface-to-surface interactions that occur as a result of periodic boundary conditions [15,57]. The size of the slab region (region containing atoms) is also sufficiently large to eliminate the influence of surfaces on the GB [15,57]. Moreover, in the direction parallel to the GB plane, it comprises a 2×2 supercell of the $\Sigma5(310)$ GB's unit cell. This is necessary to generate an AFMD structure along the [001] axis direction. Additionally, there was no relaxation of the cells. Only the atomic positions were relaxed. This resulted in a GB model that strongly reflects the properties of the cubic AFMD γ-Fe with varying interlayer distances in the [001] direction. For example, the fifth atomic layer from the GB center had interlayer distances of 1.82 and 1.72 Å in the [001] direction, which were close to the bulk interlayer distance. As a result, the cell dimensions of the GB model are 7.08 Å × 11.2 Å × 30.0 Å and it consists of 112 atoms. In Fig. 1, the indices 1–4 represent the equivalent GB sites. The red atoms with u (meaning up) indices are Fe atoms with positive magnetic moments, and the blue atoms with d (meaning down) indices are Fe atoms with negative magnetic moments.

The GB energy of the obtained $\Sigma5(310)$ GB ($1.24\ \mathrm{J/m^2}$) is relatively high, although the Σ value is small [41]. For example, the GB energy of this GB is comparable to that of $\Sigma29(520)$ GB ($1.29\ \mathrm{J/m^2}$) with the magnetic state of AFMD [41], whose Σ value is close to the general GB of polycrystals. There are no experimental data on the GB energy of pure γ-Fe polycrystalline. On the other hand, in the fcc metal Cu, the polycrystalline GB energy is $0.65\ \mathrm{J/m^2}$ [58], while the $\Sigma5(310)$ GB energy is $0.88\ \mathrm{J/m^2}$ [59], which is slightly higher than that of the polycrystalline Cu. The dependence of the GB energy of the [001] symmetric tilt GB of γ-Fe on the GB character is similar to that of Cu [41,60], implying that the GB energy of the $\Sigma5(310)$ GB of γ-Fe is slightly higher than that of γ-Fe polycrystalline. Thus, in terms of GB energy, the $\Sigma5(310)$ is a reasonable GB model for describing fracture at polycrystalline GB. Indeed, using FPCTTs, the $\Sigma5(310)$ GB was used in a systematic investigation of solute elements at Cu GBs [59,61]. Although there are few experimental results on the GB segregation energies of solute elements in γ-Fe [4], the GB segregation energies of Mo and Mn at general GBs (prior γ GBs) in γ-Fe polycrystalline have been determined based on the results of atom probe tomography [62]. The Mo and Mn segregation energies calculated using the $\Sigma5(310)$ GBs with the AFMD magnetic states created by the above procedure reproduce their experimental values well [41]. Moreover, due to its low Σ value, the $\Sigma5(310)$ GB model developed above is simple to calculate and is a reasonable GB model that approximates GB fracture in γ-Fe polycrystalline in terms of GB energy and GB segregation.

To determine the segregation sites of Zn, the segregation energies of Zn substitution for Fe in sites $1u$-$4u$ were calculated. The segregation energy calculation is based on the energy of Zn substitution for Fe at site B in the bulk model shown in Fig. 1(c). In the GB model with Zn segregation, the atoms near the surfaces were fixed to the same coordinates as in the GB model without solute elements, and only the atomic coordinates of the remaining atoms were relaxed to make the slab part consistent with the size of the slab part in the GB model without solute elements for the FPCTT described below. The segregation energies were –0.31, –0.04, 0.04, and 0.00 eV for $1u$, $2u$, $3u$, and $4u$, respectively, with site $1u$ being the most stable. Notably, the case where Zn is placed at sites $1d$-$4d$ is equivalent to the case where Zn is placed at sites $1u$-$4u$, respectively. To maintain the symmetry of the magnetic states in the GB model, a GB model in which Fe is substituted by Zn at all four sites equivalent to site $1u$ was used. Even with four Zn sites, the interaction among Zn atoms was small and the segregation energy per atom was -0.34 eV. Moreover, the high solubility of Zn in γ-Fe [63] indicates that these segregation energies calculated by first-principles are reasonable [64], as discussed in detail in Sec. III B.

Furthermore, FPCTTs were performed on the GB without solute elements (clean GB) and GB with Zn segregation (GB with Zn) using the method proposed by Tian *et al.* [40]. The atoms at both ends of the GB model were fixed, and strain was applied by displacing the atoms in a direction perpendicular to the GB. The uniaxial tensile engineering strain was applied in the direction of the [310] axis at 1.67% (0.25 nm) for each strain step. The cell size was fixed and only the atomic coordinates were relaxed. In other words, the Poisson effect (i.e., the effect of lateral contraction) [40,65] was disregarded. However, even when the Poisson effect is ignored, FPCTTs can semiquantitatively reproduce the experimental results on the GB strengthening/embrittlement effect of solute elements [13–17]. Additionally, by fixing the cell size, the FPCTTs strongly reflect the properties of the AFMD γ-Fe with cubic symmetry. It is worth noting that the stress state in the FPCTT is different from that in the experimental tensile test. Based on the calculation results, the validity of this treatment is discussed in detail in Sec. III B. The uniaxial tensile stress was calculated by dividing the change in energy at each strain by the change in volume of the slab region at each strain. As the tensile strain increases, the stress increases, and the stress drops rapidly to less than zero when it reaches a certain strain level. This is referred to as GB fracture. The GB fracture energy was defined as the difference between the maximum energy of the system during the tensile process and the energy of the system without strain. Meanwhile, the GB fracture stress was determined as the maximum stress up to the GB fracture. The strain just before the GB fracture was defined as the fracture strain.

To analyze the change in electronic state in response to the applied strain, we employed COHP analysis [46–49], which describes the contribution of local interatomic bonding in a solid, such as solute–Fe and Fe–Fe bonds, via the intersite representation of the band-structure energy by an atomic-orbital basis set. This analysis is performed by projecting conventional plane-wave functions onto an atomic-orbital basis set, as a projected COHP (pCOHP). Moreover, the -ICOHP, which is calculated by integrating the pCOHP up to the Fermi energy and flipping the sign, can be used to numerically evaluate the contribution of atomic-orbital pairs to the reduction of the band-structure energy, i.e., the magnitude of covalent-bonding contribution. The COHP analysis was performed using LOBSTER [48], while the pbeVaspFit2015 basis set [48] was used for the basis functions of the following: Zn:$4s$, $4p$, $3d$; Fe: $4s$, $4p$, and $3d$.

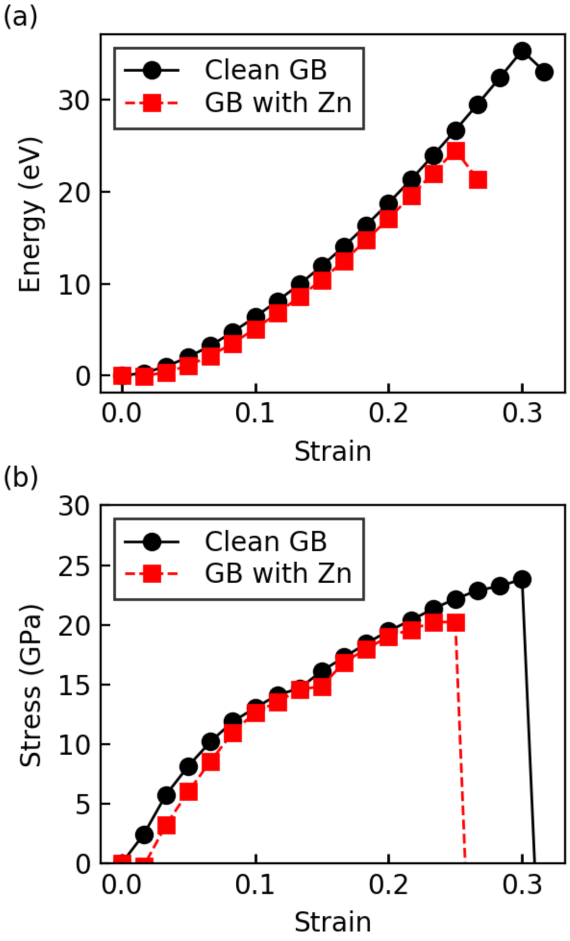

FIG. 2. (a) Energy vs strain and (b) stress vs strain for the clean GB and the GB with Zn.

III. RESULTS AND DISCUSSION

A. Effect of Zn on GB fracture in γ-Fe and its electronic origin

Figure 2 shows the stress-strain relationship and energy-strain relationship revealed by FPCTTs on clean GB and GB with Zn segregation, respectively. The fracture strain and GB fracture stress of the clean GB were 30.0% and 23.8 GPa, respectively, while those of the GB with Zn segregation were lower (25.0% and 20.2 GPa, respectively). The GB with Zn segregation also had a lower GB fracture energy than the clean GB. By examining the difference in the stress-strain relationship between the two GB models, it is clear that the stress rises more slowly in the GB with Zn segregation at strains less than 10%. This is because Zn segregation expands the lattice slightly in the direction of tensile strain. The stress-strain relationship is similar to that in the clean GB in the strain range of 10–20%. However, from around as strain was increased from ∼20%, the stress in the GB with Zn began to decrease compared to that in the clean GB, and GB fracture occurred at relatively small strain and stress. Thus, Zn segregation promoted the GB fracture in γ-Fe. We then discuss the electronic origin of how the Zn segregation promotes GB fracture.

To analyze the effect of Zn on the GB fracture, we first identify the bonds that initiate the fracture. Figures 3 and 4 show the changes in the GB structure and bond length between atoms near the GB center, respectively, with tensile strain. Focusing on the clean GB shown in Fig. 4, the bond length without strain is larger for antiferromagnetic bonds between Fe atoms with different magnetic moments than for ferromagnetic bonds between Fe atoms with the same magnetic moment. The increase in bond length with increasing strain is also larger for the antiferromagnetic bonds, and is the largest for the Fe $(1u)$–Fe $(4d)$ bond, where the bond length is roughly proportional to the strain. This large increase in bond length with increasing strain is related to the fact that the bond length without strain is large owing to lattice distortion near the GB center and that the direction of the bond is close to the direction of tensile strain. The GB structure during structural relaxation at 30% strain (Fig. 3) also indicates that GB fracture was caused by the breaking of this bond. In the GB with Zn, the bond length at each strain tends to be slightly larger for the bond between Zn and Fe with a down magnetic moment. As in the clean GB, the Zn $(1u)$–Fe $(4d)$ bond shows a large increase in bond length with increasing strain, and GB failure occurs at a strain where this bond length exceeds 3.6 Å. The GB structure during the structural relaxation at a strain of 26.7% (Fig. 3) also indicates that the GB fracture was caused by the breaking of this bond. Thus, in both clean GB and GB with Zn segregation, GB fracture is caused by the breaking of bonds with large bond lengths near the GB center and bond directions close to the direction of tensile strain.

Next, to elucidate the effect of Zn on each bond, we focus on the difference in strain dependence of the bond length between the clean GB and GB with Zn segregation. The Fe–Fe bond length at each strain tends to be larger for antiferromagnetic bonds than for ferromagnetic bonds. At strains below 20%, most of the bond length between Zn $(1u)$ and Fe is located between them. In this strain range, the strain dependence is similar for the bond lengths of Fe $(1u)$–Fe $(4d)$ and Zn $(1u)$–Fe $(4d)$, which were the starting points of fracture in the respective GB models. However, when strain exceeded 20%, the increase in the Zn $(1u)$–Fe $(4d)$ bond length became larger than that of the Fe $(1u)$–Fe $(4d)$ bond length; the bond length exceeded 3.6 Å at smaller strain, resulting in GB fracture. The 20% strain is consistent with the strain at which the stress in the GB with Zn segregation begins to decrease, relative to that in the clean GB, suggesting that enhancement of GB fracture by Zn segregation is brought about through these bonds. Comparing Fe $(1u)$–Fe $(3d)$ with Zn $(1u)$–Fe $(3d)$ and Fe $(1u)$–Fe $(2d)$ with Zn $(1u)$–Fe $(3d)$, the increase in bond length with increasing strain is smaller for Zn–Fe bonds than for Fe–Fe bonds up to a strain of less than 20%. This indicates that Zn segregation has little effect on promoting fracture through these bonds. On the other hand, for Fe $(3u)$–Fe $(-3\mathrm{u})$ bonds adjacent to Fe $(1u)$ or Zn $(1u)$, the increase in bond length versus strain in GB with Zn segregation is significantly larger than that in clean GB when the strain exceeds 20%. This suggests that Zn segregation also weakens the neighboring Fe–Fe bonds.

The effect of Zn on each bond in connection with the electronic structure is discussed based on the strain dependence of the -ICOHP between the bonds shown in Fig. 4 (Fig. 5). The strain dependence of the bond length corresponds to that of the -ICOHP: the larger the bond length, the smaller the

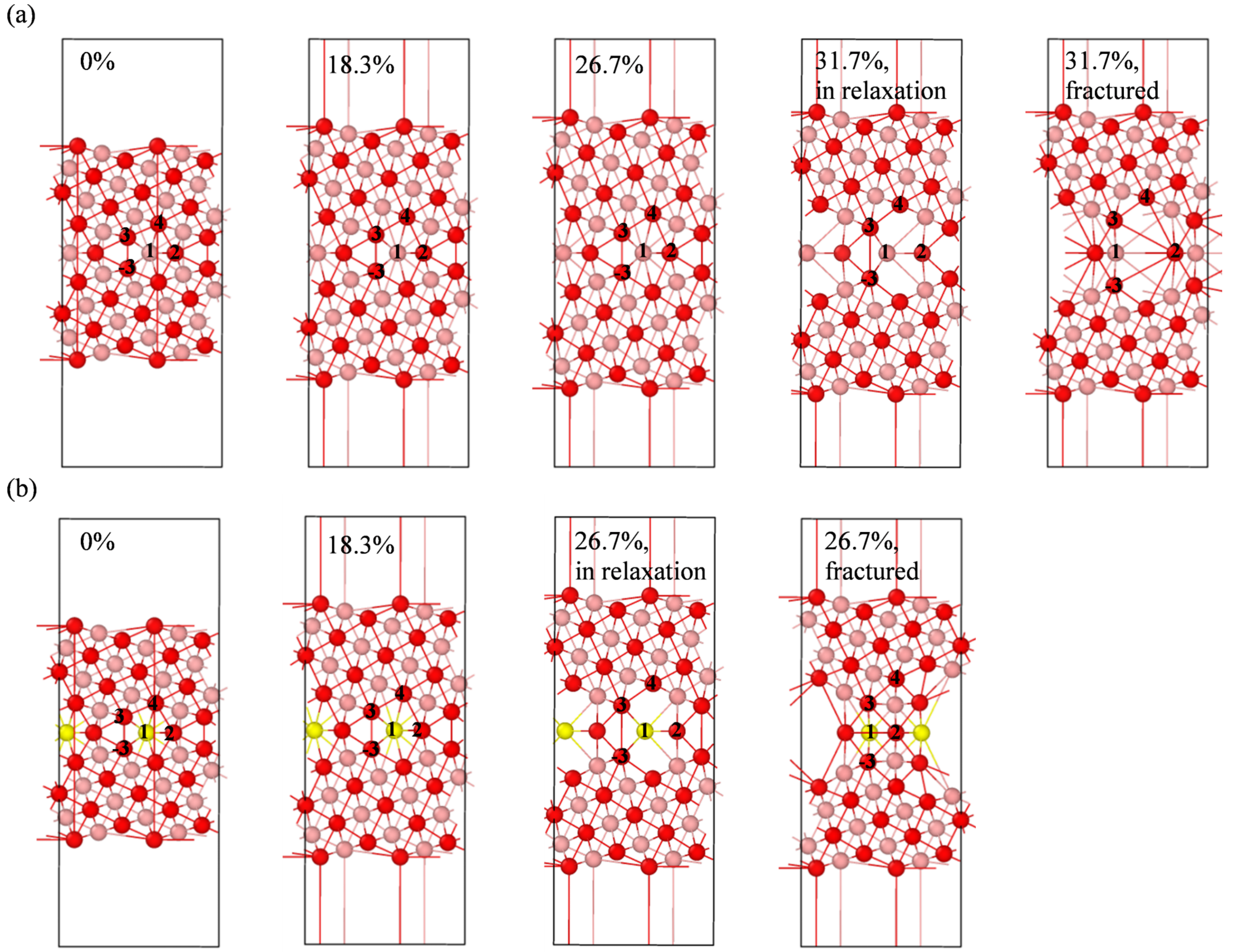

FIG. 3. Changes in atomic structure of (a) the clean GB and (b) the GB with Zn during FPCTTs. The atomic structure of the clean GB during the structural relaxation at 31.7% strain is also shown in (a). The atomic structure of the GB with Zn during the structural relaxation at 26.7% strain is also shown in (b).

-ICOHP tends to be. First, we focus on the difference between the Fe (1*u*)–Fe (4*d*) and Zn (1*u*)–Fe (4*d*) bonds, which is the origin of the fracture. Notably, the scale of the vertical axis of these bonds are different from that of the other bonds shown in Fig. 5. In the low-strain region, the -ICOHP is smaller in Zn (1*u*)–Fe (4*d*) than in Fe (1u)–Fe (4*d*), but after 10% strain, the -ICOHPs are similar. However, when the strain exceeds 20.0%, the -ICOHP of Zn (1*u*)–Fe (4*d*) becomes significantly smaller than that of Fe (1*u*)–Fe (4*d*).

Comparing Fe (1*u*)–Fe (2*d*) with Zn (1*u*)–Fe (2*d*) and Fe (1*u*)–Fe (3*d*) with Zn (1*u*)–Fe (3*d*), no significant change is observed at 21.6% strain, and the -ICOHP of Zn–Fe is larger than that of Fe–Fe. At strains below 20%, the -ICOHP of the Fe (3*u*)–Fe (−3*u*) bond adjacent to Zn is almost the same in both the clean GB and the GB with Zn segregation. As the strain increased above 20.0%, the decrease in the -ICOHP of Fe (3*u*)–Fe (−3*u*) is larger for the GB with Zn segregation than for the clean GB. The -ICOHP of Fe (3*u*)–Fe (−3*u*) just before the GB failure is more than 1.0 eV, much larger than that of Zn (1*u*)–Fe (4*d*) (0.4 eV). This result confirms that the fracture in the GB with Zn segregation originated from the Zn (1*u*)–Fe (4*d*) bond. On the other hand, the increase in bond length and decrease in -ICOHP of Fe (3*u*)–Fe (−3*u*) adjacent to Zn at strain above 20% might lead to a conclusion that Zn weakened the bond of Fe (3*u*)–Fe (−3*u*), which promoted the GB fracture. For example, Cu in α-Fe has been shown to weaken Fe–Fe bonds by depriving neighboring Fe of electrons and reducing the number of electrons contributing to the Fe–Fe bond [66]. However, such an effect reduces the electron density in the Fe–Fe interstitial region from the unstrained state and significantly enhances the change in bond length with strain from the low-strain region. On the other hand, in the low-strain region, the bond length and -ICOHP between Fe (3*u*)–Fe (−3*u*) are almost the same in the clean GB and the GB with Zn segregation. At strains above 20%, the increase in the bond length of Zn (1*u*)–Fe (4*d*) becomes larger than that of Fe (1*u*)–Fe (4*d*). These results indicate that Zn has little effect on weakening the bond between adjacent Fe (3*u*)–Fe (−3*u*). Therefore, it can be interpreted that the Zn (1*u*)–Fe (4*d*) bond length increases rapidly when the strain exceeds 20% in the GB with Zn, which elongates the Fe (3*u*)–Fe (−3*u*) bond, which is parallel to the strain direction.

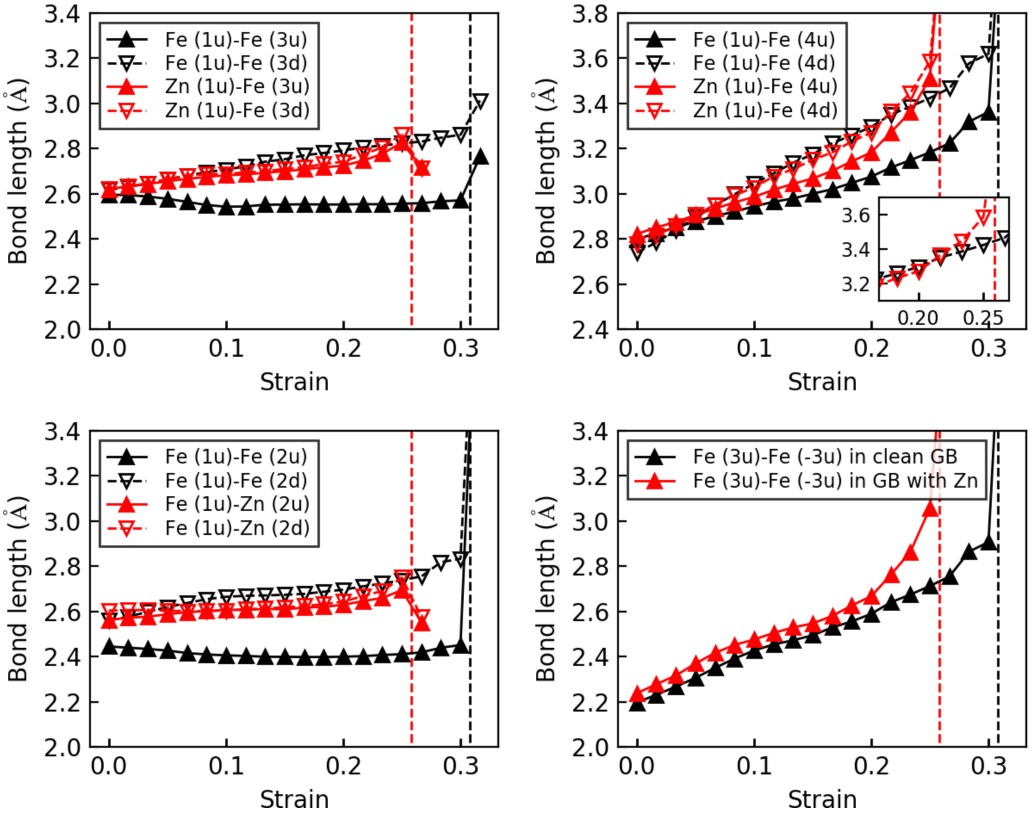

FIG. 4. Variation of bond length with strain between atoms near the GB center. The black plots represent the bonds in the clean GB, and the red plots represent the bonds in the GB with Zn. The black and red vertical dashed lines represent the strains at which GB fracture occurs in the clean GB and the GB with Zn, respectively.

The strain dependence of the bond length and -ICOHP of each bond indicates that the GB embrittlement caused by Zn segregation is mainly caused by the difference in nature between the Zn $(1u)$–Fe $(4d)$ and Fe $(1u)$–Fe $(4d)$ bonds. Therefore, to interpret the decrease in -ICOHP observed near 20.0% strain in Zn $(1u)$–Fe $(4d)$, the electronic structure of this bond is discussed in detail. Figure 6(a) shows the COHPs of Fe $(1u)$–Fe $(4d)$ and Zn $(1u)$–Fe $(4d)$ at strains of 0.0, 18.3, 20.0, 21.7, and 25.0%. Meanwhile, Fig. 6(b) shows the -ICOHPs obtained by integrating the COHPs up to the corresponding energy on the horizontal axis at 0.0, 18.3, 20.0, 21.7, and 25.0% strain. There are negative COHPs near -7 eV in the Zn $(1u)$–Fe $(4d)$ COHP, i.e., bonding orbitals, where the occupation of electrons contributes significantly to the -ICOHP. Therefore, at all strain levels except the 25% fracture strain, the -ICOHP, which integrates the COHP up to around -3 eV, is larger for Zn $(1u)$–Fe $(4d)$ than for Fe $(1u)$–Fe $(4d)$. On the other hand, because the COHP of Fe $(1u)$–Fe $(4d)$ is negative in comparison to that of Zn $(1u)$–Fe $(4d)$ at energy levels above -3 eV, the -ICOHPs of Fe $(1u)$–Fe $(4d)$ and Zn $(1u)$–Fe $(4d)$ integrated up to 0 eV are similar for strains of 18.3 and 20.0%. To compare Fe $(1u)$–Fe $(4d)$ and Zn $(1u)$–Fe $(4d)$ in more detail, Fig. 7 shows the difference in -ICOHP obtained by integrating the difference between the COHPs of Fe $(1u)$–Fe $(4d)$ and Zn $(1u)$–Fe $(4d)$ up to the corresponding energy on the horizontal axis. Positive values mean that the -ICOHP of Zn $(1u)$–Fe $(4d)$ is larger than that of Fe $(1u)$–Fe $(4d)$. The -ICOHP difference near -7 eV and at 0 eV is almost the same between 18.3 and 20.0%, but decreases at 21.7%. At this strain, the -ICOHP difference generated by integration up to around -7 eV is maintained as the -ICOHP difference when integrated up to 0 eV. This indicates that the decrease in -ICOHP difference when the strain increases from 20.0 to 21.7% is due to the change in the COHP of Zn $(1u)$–Fe $(4d)$ near -7 eV, which corresponds to the change in electron occupation to the bonding orbital.

To further discuss the electronic origin of the change in COHP between Zn $(1u)$–Fe $(4d)$ near -7 eV, Fig. 8 shows the COHPs between Fe $(1u)$–Fe $(4d)$ and the LDOSs of Fe $(1u)$ and Fe $(4d)$ in the clean GB at 0, 20.0, 21.7, and 25.0% strain. The metallic bonding between Fe $(1u)$ and Fe $(4d)$ is formed over a wide energy range, mainly due to the hybridization between the $3d$ orbitals. Figure 9 shows COHPs between Zn $(1u)$–Fe $(4d)$ and LDOSs of Zn $(1u)$ and Fe $(4d)$ in the GB with Zn at 0, 20.0, 21.7, and 25.0% strain. The comparison of COHP and LDOS at 0.0% strain shows that the Zn $(1u)$–Fe (4d) bonding around -7 eV is a covalent-like coupling between the $3d$ orbitals of Zn $(1u)$ and Fe $(4d)$. When the COHP is integrated up to the Fermi energy, the ICOHP of Fe $(1u)$–Fe $(4d)$ is comparable to that of Zn $(1u)$–Fe $(4d)$, because an antibonding orbital is formed near the Fermi energy and is occupied in the minority spin between Zn $(1u)$–Fe $(4d)$. The COHP and LDOS show that the $3d$ orbitals of Zn are localized in the deep-energy region, which means that the $3d$ orbitals of Zn are more localized in the nucleus than those of Fe. Therefore, it becomes difficult for the Fe–Zn bond

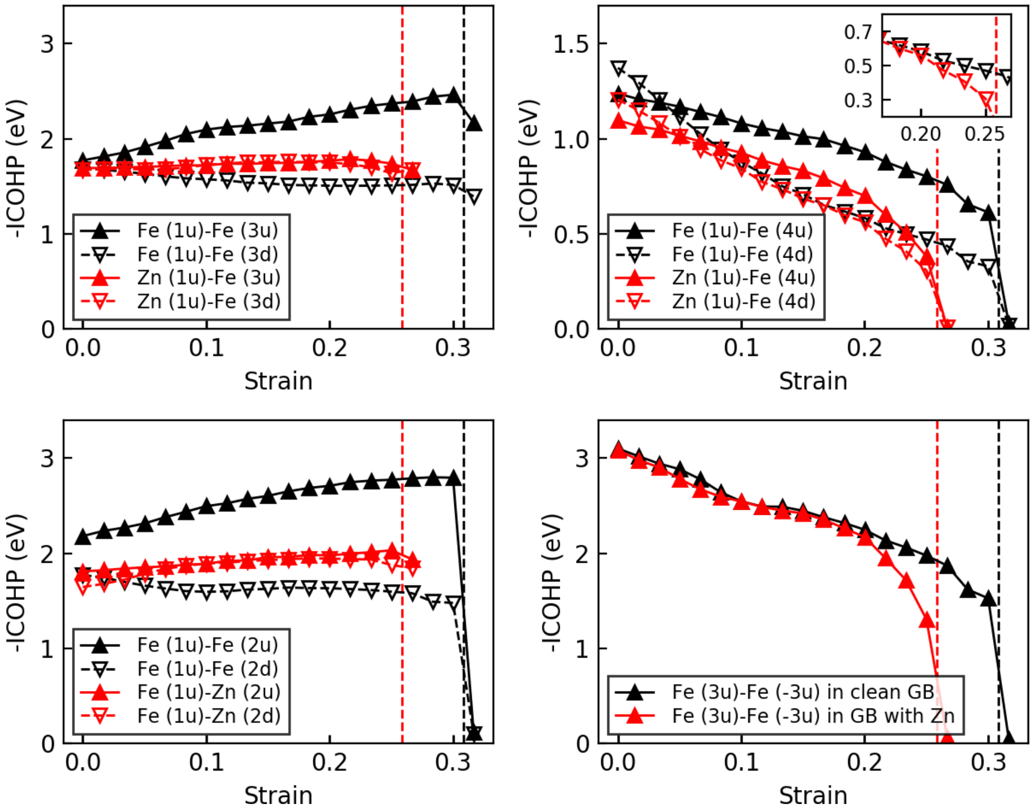

FIG. 5. Variation of -ICOHP between atoms near the GB center with strain. The black and red plot shows the -ICOHP of bonds in the clean GB and in the GB with Zn, respectively. The black and red vertical dashed lines represent the strains at which GB fracture occurs in the clean GB and the GB with Zn, respectively.

to hybridize orbitals at smaller strains than the Fe–Fe bond, resulting in lower -ICOHP and GB fracture at a lower stress and a smaller strain. Thus, by employing COHP analysis on FPCTTs, we can quantify the change in bond length and band-structure energy numerically and discuss its electronic origin in detail.

As described above, FPCTT results using γ-Fe GBs in the AFMD are consistent with Zn-induced GB embrittlement and allowed us to interpret its electronic origin. The enhancement of GB fracture by Zn is caused by the fact that the covalent-like bonds between the $3d$ orbitals of Fe and Zn near the GB center are broken at smaller strains and lower stresses than that

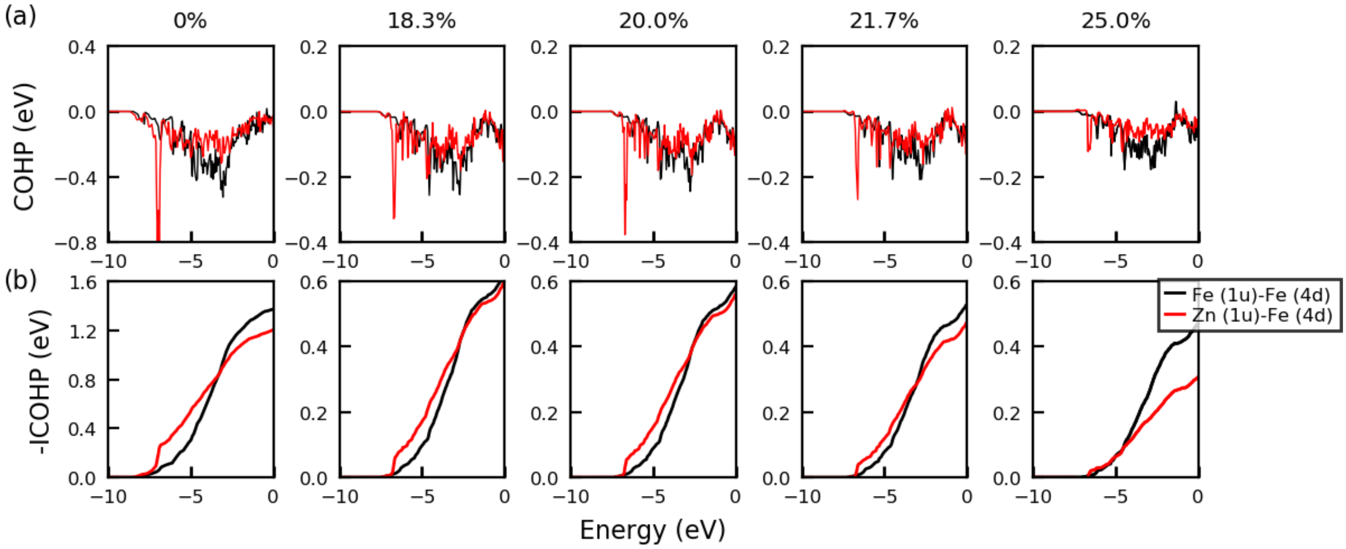

FIG. 6. (a) COHPs of Fe ($1u$)–Fe ($4d$) and Zn ($1u$)–Fe ($4d$) at strains of 0.0, 18.3, 20.0, 21.7, and 25.0%. (b) -ICOHPs obtained by integrating the COHPs up to the corresponding energy on the horizontal axis at 0.0, 18.3, 20.0, 21.7, and 25.0% strain. The black and red lines show the bond in the clean GB and in the GB with Zn, respectively.

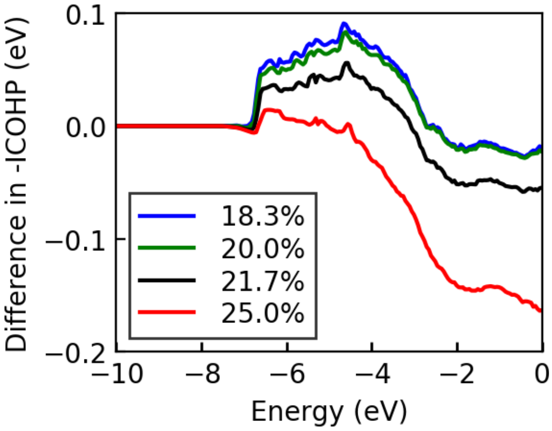

FIG. 7. Difference in -ICOHP obtained by integrating the difference between the COHP of Fe (1*u*)–Fe (4*d*) and Zn (1*u*)–Fe (4*d*) up to the corresponding energy on the horizontal axis. Positive values mean that the -ICOHP of Zn (1*u*)–Fe (4*d*) is larger than that of Fe (1*u*)–Fe (4*d*).

of the Fe–Fe bonds due to the localization of the 3*d* orbital of Zn in γ-Fe. This embrittlement mechanism is highly general and may be applicable to GBs other than the $\Sigma5(310)$ GB.

Lastly, the relationship between our calculations and the analysis of Peng *et al.* [17] about the effect of Zn on GB fracture in α-Fe will be discussed. In their analysis of α-Fe GBs, FPCTT were performed on a $\Sigma5(100)$ GB with a monatomic layer of Zn segregated at the most stable site. In α-Fe, Zn reduces the GB fracture stress and the GB fracture energy, which qualitatively corresponds to our calculations for γ-Fe. On the other hand, in the $\Sigma5(001)$ GB of α-Fe, the GB fracture stress is reduced from 21 to 14 GPa by Zn, and this reduction is significantly larger than that in the $\Sigma5(310)$ GB of γ-Fe. In α-Fe, the bond length of Fe–Zn is larger than the Fe–Fe bond length, and the difference in bond lengths increases with increasing strain. Furthermore, the bond length of Fe–Fe adjacent to Zn is larger than that in clean GB without strain, and the increase in bond length compared to that in clean GB becomes more pronounced with increasing strain. From these results, the Zn-induced fracture enhancement of α-Fe GBs is arguably caused by the increase in the Zn–Fe bond length and the weakening of the Fe–Fe bond due to the reduced electron density between the Fe atoms adjacent to Zn [17]. In the γ-Fe GB, the bond length of Fe–Zn is almost the same as that of the antiferromagnetic Fe–Fe bond, or even smaller. On the other hand, the Fe–Zn bond length is larger than ferromagnetic Fe–Fe bonds, which is similar to the behavior in α-Fe GBs. These results indicate that the effect of Zn is different, depending on the magnetic state between α-Fe and γ-Fe. In $\Sigma5(310)$ of γ-Fe, the Fe–Fe bond adjacent to Zn is hardly weakened compared to the clean GB based on the bond length and the variation of -ICOHP with strain. In addition, Chen *et al.* [39] recently showed that Zn lowers the cohesive energy of the γ/α interface based not on FPCTTs but on changes in the γ/α interface and surface energies due to the presence of Zn. They argued that the change in cohesive energy is due to the weakening of the Fe–Fe bonds as Zn reduces the electron density between Fe atom pairs across the γ/α interface. However, at least without solute elements, all Fe atoms on the γ-Fe side near the γ/α interface are ferromagnetic in these calculations, i.e., the direction of their magnetic moment is the same as that of the Fe atoms on the α-Fe side. Therefore, as in the case of the α-Fe GB, Zn may have reduced the electron density between adjacent Fe–Fe atoms. These results suggest that the decrease in electron density between Zn and adjacent Fe–Fe also reflects the difference in the magnetic state of the two phases. However, since the decrease in electron density does not necessarily imply weakening of the bonds, a detailed analysis of the α-Fe GB by FPCTT and COHP is also necessary. Although it is difficult to make an exact comparison between α-Fe and γ-Fe because the bulk and grain boundary crystal structures depend on the magnetic state, this study shows that the difference in magnetic state affects the quantitative influence of the solute elements on the GB fracture and its electronic origin.

B. Validity and future developments of FPCTTs on γ-Fe GBs using the AFMD

In this section, we discuss the validity of FPCTTs on γ-Fe GBs using the AFMD in terms of the treatment of the magnetic state of γ-Fe. In FPCTTs, magnetism played an important role in studies on Ni GBs [40]. Specifically, when the ferromagnetism of Ni is not considered and it is treated as nonmagnetic, the GB fracture energy and fracture stress are overestimated. In addition, the nonmagnetic calculation also overestimates the effect of the decrease in the GB fracture stress of Ni GBs by S segregation. Based on these results, it is argued that the effects are even more pronounced when the magnetic moment is larger than that of Ni, as in Fe [40]. Therefore, in the FPCTT of γ-Fe, properly considering the magnetism of Fe is necessary in the calculations.

To begin, we discuss the validity of the approximation using the AFMD for paramagnetic γ-Fe GBs without tensile strain. The magnetic structure of γ-Fe with an fcc crystal structure exhibits a spin-spiral magnetic ground state [67–69]. Additionally, the effectiveness of magnetic structures that assign positive and negative magnetic moments to each Fe atom based on special quasirandom structures (SQSs) [70] has been demonstrated in the calculation of solute elements in paramagnetic γ-Fe bulk [71]. These magnetic states, however, cannot be applied directly to GBs. The AFMD state is the most stable collinear state in γ-Fe with an fcc crystal structure [44]. In particular, the lattice constants and elastic properties of the AFMD γ-Fe with cubic symmetry and varying interlayer distances in the [001] direction are similar to those of paramagnetic γ-Fe [42,50,51]. Additionally, the bonding state with surrounding Fe atoms when solute elements are placed in the bulk is also very similar to that of SQS [41,51]. In γ-Fe with the AFMD magnetic structure, the tetragonal crystal structure is known to have lower energy than the cubic one [43,69], but the consideration of atomic positional relaxation reduces the energy difference to only about 20 meV/atom [42,72]. In the current study, we constructed the GB model with fixed cell size using the lattice constants of the cubic AFMD γ-Fe. The GB model with the fixed cell size strongly reflects the properties of the cubic AFMD γ-Fe. For example, the fifth atomic layer from the GB center had interlayer distances of 1.82 and 1.72 Å in the [001] direction,

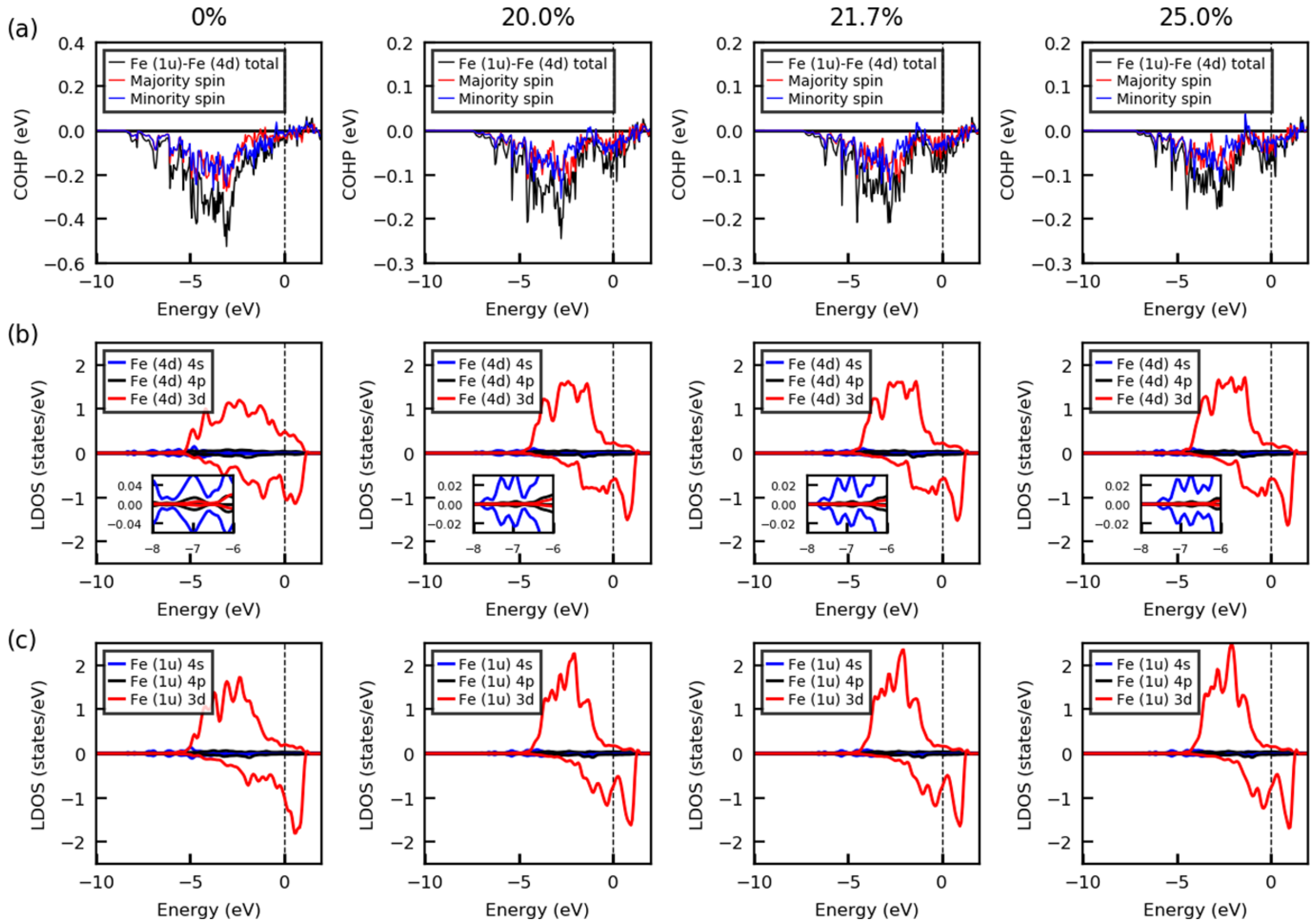

FIG. 8. (a) COHPs between Fe ($1u$)–Fe ($4d$) and (b) LDOSs of Fe ($1u$) and (c) Fe ($4d$) in the clean GB at 0, 20.0, 21.7, and 25.0% strain.

which were close to the bulk interlayer distance. Additionally, the fact that the obtained $\Sigma5(310)$ GB model well reproduces the GB segregation in paramagnetic γ-Fe [41] indicates that the atomic structure near the GB center is a good approximation of paramagnetic γ-Fe. Thus, our GB model approximates the paramagnetic γ-Fe GB well, at least in the strain-free state.

Then, we discuss the case where tensile strain is considered. In the elastic range corresponding to relatively small strains, the elastic properties of the AFMD γ-Fe are shown to be closest to those of paramagnetic γ-Fe [50]. This demonstrates the validity of our calculation method, which accurately reflects the properties of AFMD γ-Fe. The validity of the AFMD in terms of behavior beyond the elastic range to fracture will be discussed based on the calculations presented in the previous section. Figure 10 shows the dependence of the magnetic moment of Fe atoms near the GB center on strain in the clean GB. The magnetic moments of all Fe atoms increased with increasing strain, i.e., with increasing bond length with neighboring Fe atoms. This is due to the magnetovolume effect, which corresponds well to the behavior in α-Fe [16]. The magnetic moments of all Fe atoms do not flip in response to strain, and the paramagnetic state is maintained. Owing to the symmetry of the magnetic state of the AFMD, the magnitudes of the magnetic moments of Fe ($1u$) and Fe ($1d$), for example, are the same. Additionally, as illustrated in Fig. 2, the energies and stresses in both GB models continuously vary up to the point of fracture. Thus, as a result of our method, stable FPCTTs for γ-Fe GBs were obtained. By considering the magnetic state, the response to strain depends on the orientation of the magnetic moment in Fe–Fe bond, as shown in Figs. 4 and 5. In γ-Fe, the volume modulus is higher in ferromagnetic than in the AFMD [44], which agrees well with our result. These results indicate that the γ-Fe in the AFMD can properly consider the dependence of magnetic moment of Fe and the Fe–Fe bonds on tensile strain.

We discuss the effect of the magnetic state on the GB fracture. As discussed in the previous section, antiferromagnetic bonds between Fe atoms with different magnetic moments have larger bond lengths than ferromagnetic bonds, and the increase in bond length with increasing strain is also larger, which leads to GB failure. Thus, the consideration of the magnetic state of Fe plays an important role in the GB fracture of γ-Fe. The ferromagnetic and antiferromagnetic bonds across the GB center should then have approximately the same ratio to describe the GB fracture in paramagnetism in FPCTTs. The γ-Fe GB models with [001] tilt GBs with the AFMD magnetic states achieve this with a relatively small number of atoms, as shown in Fig. 10. Therefore, the GB model and the magnetic state used in this study are reasonable approximations for investigating the GB fracture of γ-Fe using first-principles calculations, which hardly handle a large number of atoms.

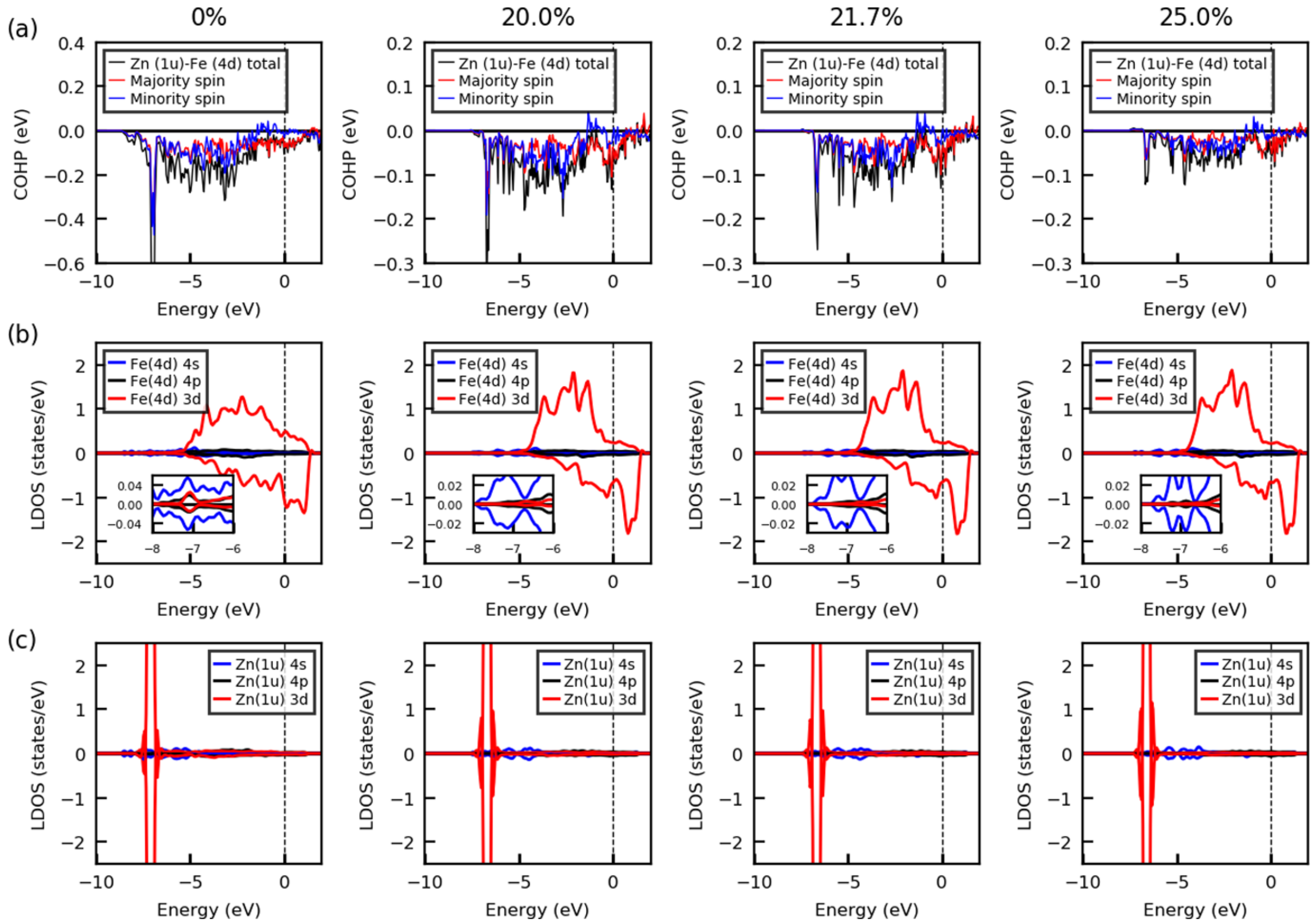

FIG. 9. (a) COHPs between Zn (1*u*)–Fe (4*d*) and (b) LDOSs of Zn (1*u*) and (c) Fe (4*d*) in the GB with Zn at 0, 20.0, 21.7, and 25.0% strain.

The initial structure of the GB model was determined using the cubic AFMD γ-Fe lattice constant, and while the atomic positions were relaxed, the cell size was not. As a result, the stress parallel to the GB plane caused by Zn segregation was not mitigated sufficiently. This effect has not been considered even in numerous studies using the FPCTT for α-Fe [13–17], but it may have an effect on the conclusions drawn. As detailed in the Supplemental Material [73], we evaluated this effect. By varying the cell sizes in a directions parallel to the GB plane and relaxing the atomic positions, we relaxed the initial structure of the GB model. To reflect the cubic symmetry, the cell sizes were varied in the same ratio in both directions. The FPCTTs were then conducted on the two GB models obtained. The results indicate that relaxation of the cell structure has a slight effect on the GB fracture stress and strain, and has no effect on the conclusion that Zn promotes GB fracture and its mechanism. These FPCTTs did not account for the Poisson effect. Even when the Poisson effect is ignored, it has been demonstrated that FPCTTs can semiquantitatively reproduce experimental results on the GB strengthening/embrittlement effect of solute elements [13–17,65], but evaluating the effect of the Poisson effect will require additional work. As previously stated, although the FPCTT for γ-Fe GBs using the AFMD does not completely describe the GB fracture of paramagnetic γ-Fe, it is a reasonable approximation for investigating the fracture of γ-Fe GBs using first-principles calculations, which are difficult to handle large atomic numbers. Our method can be used to evaluate the effect of various solute elements other than Zn on GB strengthening/embrittlement of γ-Fe GBs, as well as to investigate their electronic origin by appropriately considering the effect of paramagnetic magnetic states. There are few experimental studies on the GB strengthening/embrittlement

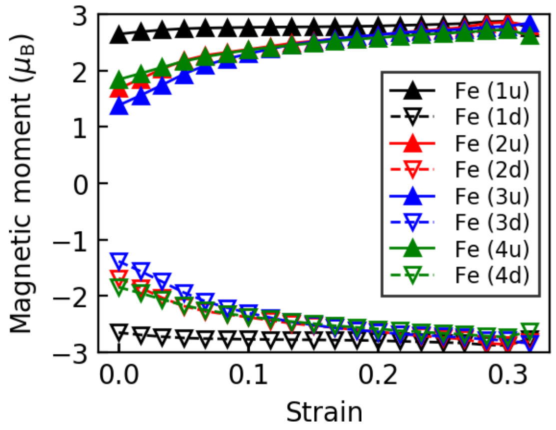

FIG. 10. Strain dependence of the magnetic moment of Fe atoms near the GB center.

effects of solute elements on γ-Fe because γ-Fe is a stable phase at high temperatures [74]. In the future, the validity of this calculation method would be verified by comparing it with experimental results for solute elements other than Zn, but this calculation method can be used to solve the problem of GB cracking at γ-Fe GBs and provide insights into the development of high-strength steels. In addition, this study shows the usefulness of COHP analysis for the analysis of electronic states in FPCTTs. This knowledge is useful for the first-principles tensile analyses of γ-Fe GBs as well as various metal GBs, which will accelerate studies on the electronic origin of GB fracture.

Finally, we discuss the validity of the Zn segregation energy at the γ-Fe GB obtained in this study. As mentioned previously, for solute elements with high solubility, the segregation energies calculated using first-principles calculations have been shown to reproduce experimental results well [64]. Zn has a high solubility limit in γ-Fe, for example, about 6.0 at. % at 1150 °C [63], which supports the calculated segregation energy. There are no published data on the segregation energy of Zn in γ-Fe. On the other hand, Lejček *et al.* calculated the segregation enthalpies of Zn for special, vicinal, and general GBs in α-Fe to be -0.02, -0.06, and -0.12 eV, respectively, using a thermodynamic model of GB segregation [75]. These segregation enthalpies are less than the segregation energy of the most stable site in the AFMD γ-Fe $\Sigma5(310)$ GB (-0.34 eV). Moreover, Scheiber *et al.* calculated the segregation energies of Zn at the $\Sigma3(111)$, $\Sigma5(310)$, and $\Sigma9(114)$ GBs in α-Fe and determined that the most stable site has segregation energy of approximately -0.60 eV at each of these GBs [38]. These segregation energies differ from those calculated by Lejček *et al.* To predict the GB segregation energy quantitatively using first-principles calculations or interatomic potentials, it is necessary to take into account the effects of bulk model size [64], segregation entropy effects [76], correction of the evaluation region for GB segregation [27,30], and the GB character and segregation site dependence of GB segregation energy [27,30,77]. Additional research into these effects is required.

IV. CONCLUSION

The FPCTTs on γ-Fe GBs considering magnetism are performed using the AFMD. The AFMD can properly account for the paramagnetism of γ-Fe, and the calculation results are consistent with experiments on grain boundary embrittlement by Zn. COHP analysis was also performed to investigate the change in electronic states during the tensile process, and the enhancement of GB fracture by Zn is found to be caused by the breaking of the covalent-like bonds between Fe and Zn at a smaller strain than the Fe–Fe bonds. This behavior is attributed to the localized nature of the $3d$ orbitals of Zn in γ-Fe. The FPCTTs of γ-Fe GBs using the AFMD is also useful for investigating the effect of various solute elements on GB fracture, providing useful insights into the development of high-strength steels. In addition, the combination of the COHP analysis and FPCTT helps elucidate the mechanisms of grain boundary strengthening/embrittlement effects of solute elements at various GBs.

ACKNOWLEDGMENT

The authors thank Nippon Steel Corporation for supporting the publication of this manuscript.

---

[1] R. Wu, A. J. Freeman, and G. B. Olson, Science **265**, 376 (1994).

[2] H. Kimura, Tetsu-to-Hagané **79**, 754 (1993).

[3] C. McMahon Jr. and L. Marchut, J. Vac. Sci. Technol. **15**, 450 (1978).

[4] P. Lejček, *Grain Boundary Segregation in Metals* (Springer Science & Business Media, Springer-Verlag, Berlin, 2010), Vol. 136.

[5] M. P. Seah, Acta Metall. **28**, 955 (1980).

[6] C. D. Horvath, in *Materials, Design and Manufacturing for Lightweight Vehicles*, 2nd ed., edited by P. K. Mallick (Woodhead Publishing, Cambridge, 2021), p. 39.

[7] D.-W. Suh and S.-J. Kim, Scr. Mater. **126**, 63 (2017).

[8] R. L. Plaut, C. Herrera, D. M. Escriba, P. R. Rios, and A. F. Padilha, Mater. Res **10**, 453 (2007).

[9] D. V. Edmonds, K. He, F. C. Rizzo, B. C. De Cooman, D. K. Matlock, and J. G. Speer, Mater. Sci. Eng., A **438–440**, 25 (2006).

[10] J. Yoo, M. C. Jo, M. C. Jo, S. Kim, S.-H. Kim, J. Oh, S. S. Sohn, and S. Lee, Acta Mater. **207**, 116661 (2021).

[11] M. Soleimani, A. Kalhor, and H. Mirzadeh, Mater. Sci. Eng., A **795**, 140023 (2020).

[12] S. Takayama, T. Ogura, S.-C. Fu, and C. J. McMahon, Metall. Trans. A **11**, 1513 (1980).

[13] M. Yuasa and M. Mabuchi, Phys. Rev. B **82**, 094108 (2010).

[14] M. Yamaguchi, K.-I. Ebihara, M. Itakura, T. Kadoyoshi, T. Suzudo, and H. Kaburaki, Metall. Mater. Trans. A **42**, 330 (2011).

[15] M. Yamaguchi, Metall. Mater. Trans. A **42**, 319 (2011).

[16] K. Ito, H. Sawada, and S. Ogata, Phys. Rev. Mater. **3**, 013609 (2019).

[17] W. Peng, H. Peng, G. Wu, and J. Zhang, Comput. Mater. Sci. **171**, 109204 (2020).

[18] H. Jin, I. Elfimov, and M. Militzer, J. Appl. Phys. **115**, 093506 (2014).

[19] K. Ito, H. Sawada, S. Tanaka, S. Ogata, and M. Kohyama, Model. Simul. Mater. Sci. Eng. **29**, 015001 (2020).

[20] E. Wachowicz and A. Kiejna, Model. Simul. Mater. Sci. Eng. **19**, 025001 (2011).

[21] Z. Xu, S. Tanaka, and M. Kohyama, J. Phys. Condens. Matter **31**, 115001 (2019).

[22] S. K. Bhattacharya, M. Kohyama, S. Tanaka, and Y. Shiihara, J. Phys. Condens. Matter **26**, 355005 (2014).

[23] M. Čák, M. Šob, and J. Hafner, Phys. Rev. B **78**, 054418 (2008).

[24] M. Kohyama, S. Tanaka, and Y. Shiihara, Mater. Trans. **62**, 1 (2021).

[25] S. M. Eich and G. Schmitz, Acta Mater. **147**, 350 (2018).

[26] M. Rajagopalan, M. A. Tschopp, and K. N. Solanki, JOM **66**, 129 (2014).
[27] K. Ito, H. Sawada, and S. Ogata, Mater. Trans. **62**, 575 (2021).
[28] K. Ito, H. Sawada, and S. Ogata, J. Japan Inst. Met. Mater. **84**, 237 (2020).
[29] K. Ito, Y. Tanaka, and H. Sawada, J. Japan Inst. Met. Mater. **85**, 421 (2021).
[30] K. Ito, Y. Tanaka, and H. Sawada, Mater. Trans. **63**, 269 (2022).
[31] H. Mohrbacher and T. Senuma, Metals **10**, 853 (2020).
[32] M. C. Jo, J. Yoo, S. Kim, S. Kim, J. Oh, J. Bian, S. S. Sohn, and S. Lee, Mater. Sci. Eng., A **789**, 139656 (2020).
[33] M. H. Razmpoosh, E. Biro, D. L. Chen, F. Goodwin, and Y. Zhou, Mater. Charact. **145**, 627 (2018).
[34] M. H. Razmpoosh, A. Macwan, E. Biro, D. L. Chen, Y. Peng, F. Goodwin, and Y. Zhou, Mater. Des. **155**, 375 (2018).
[35] M. H. Razmpoosh, B. Langelier, E. Marzbanrad, H. S. Zurob, N. Zhou, and E. Biro, Acta Mater. **204**, 116519 (2021).
[36] M. H. Razmpoosh, C. DiGiovanni, Y. N. Zhou, and E. Biro, Prog. Mater. Sci. **121**, 100798 (2021).
[37] D. Bhattacharya, L. Cho, E. van der Aa, H. Ghassemi-Armaki, A. Pichler, K. O. Findley, and J. G. Speer, Scr. Mater. **175**, 49 (2020).
[38] D. Scheiber, K. Prabitz, L. Romaner, and W. Ecker, Acta Mater. **195**, 750 (2020).
[39] Y. Chen, C. Wang, and W. Xu, Metall. Mater. Trans. A **53**, 1604 (2022).
[40] Z. X. Tian, J. X. Yan, W. Xiao, and W. T. Geng, Phys. Rev. B **79**, 144114 (2009).
[41] K. Ito and H. Sawada, Comput. Mater. Sci. 111050 (2021).
[42] N. I. Medvedeva, D. Van Aken, and J. E. Medvedeva, J. Phys. Condens. Matter **22**, 316002 (2010).
[43] D. W. Boukhvalov, Y. N. Gornostyrev, M. I. Katsnelson, and A. I. Lichtenstein, Phys. Rev. Lett. **99**, 247205 (2007).
[44] D. E. Jiang and E. A. Carter, Phys. Rev. B **67**, 214103 (2003).
[45] H. C. Herper, E. Hoffmann, and P. Entel, Phys. Rev. B **60**, 3839 (1999).
[46] V. L. Deringer, A. L. Tchougréeff, and R. Dronskowski, J. Phys. Chem. A **115**, 5461 (2011).
[47] R. Dronskowski and P. E. Bloechl, J. Phys. Chem. **97**, 8617 (1993).
[48] S. Maintz, V. L. Deringer, A. L. Tchougréeff, and R. Dronskowski, J. Comput. Chem. **37**, 1030 (2016).
[49] S. Maintz, V. L. Deringer, A. L. Tchougréeff, and R. Dronskowski, J. Comput. Chem. **34**, 2557 (2013).
[50] L. Sun, H. R. Gong, and X. Gong, J. Phys. Condens. Matter **32**, 165806 (2020).
[51] H. Jin, Atomistic simulations of solute-interface interactions in iron, Ph.D. thesis, University of British Columbia, Vancouver, 2014.
[52] G. Kresse and D. Joubert, Phys. Rev. B **59**, 1758 (1999).
[53] G. Kresse and J. Furthmüller, Phys. Rev. B **54**, 11169 (1996).
[54] J. P. Perdew, K. Burke, and M. Ernzerhof, Phys. Rev. Lett. **77**, 3865 (1996).
[55] H. J. Monkhorst and J. D. Pack, Phys. Rev. B **13**, 5188 (1976).
[56] M. Methfessel and A. T. Paxton, Phys. Rev. B **40**, 3616 (1989).
[57] Z. X. Tian, J. X. Yan, W. Hao, and W. Xiao, J. Phys. Condens. Matter **23**, 015501 (2011).
[58] T. Surholt and C. Herzig, Acta Mater. **45**, 3817 (1997).
[59] Z. Huang, F. Chen, Q. Shen, L. Zhang, and T. J. Rupert, Acta Mater. **148**, 110 (2018).
[60] M. A. Tschopp, S. P. Coleman, and D. L. McDowell, Integr. Mater. Manuf. Innov. **4**, 176 (2015).
[61] Z. Huang, F. Chen, Q. Shen, L. Zhang, and T. J. Rupert, Acta Mater. **166**, 113 (2019).
[62] J. Takahashi, K. Ishikawa, K. Kawakami, M. Fujioka, and N. Kubota, Acta Mater. **133**, 41 (2017).
[63] X. Su, N.-Y. Tang, and J. M. Toguri, J. Alloys Compd. **325**, 129 (2001).
[64] P. Lejček, M. Šob, V. Paidar, and V. Vitek, Scr. Mater. **68**, 547 (2013).
[65] M. Černý, P. Šesták, P. Řehák, M. Všianská, and M. Šob, Model. Simul. Mater. Sci. Eng. **27**, 035007 (2019).
[66] M. Yuasa and M. Mabuchi, J. Phys. Condens. Matter **22**, 505705 (2010).
[67] S. V. Okatov, Y. N. Gornostyrev, A. I. Lichtenstein, and M. I. Katsnelson, Phys. Rev. B **84**, 214422 (2011).
[68] L. Tsetseris, Phys. Rev. B **72**, 012411 (2005).
[69] M. Friák, M. Šob, and V. Vitek, Phys. Rev. B **63**, 052405 (2001).
[70] A. Zunger, S. H. Wei, L. G. Ferreira, and J. E. Bernard, Phys. Rev. Lett. **65**, 353 (1990).
[71] A. V. Ponomareva, Y. N. Gornostyrev, and I. A. Abrikosov, Phys. Rev. B **90**, 014439 (2014).
[72] K. Wang, S.-L. Shang, Y. Wang, Z.-K. Liu, and F. Liu, Acta Mater. **147**, 261 (2018).
[73] See Supplemental Material at http://link.aps.org/supplemental/10.1103/PhysRevMaterials.6.053604 for the effect of cell-size relaxation.
[74] P. Lejček, M. Šob, and V. Paidar, Prog. Mater. Sci. **87**, 83 (2017).
[75] P. Lejček and S. Hofmann, Acta Mater. **170**, 253 (2019).
[76] P. Lejček, S. Hofmann, M. Všianská, and M. Šob, Acta Mater. **206**, 116597 (2021).
[77] D. Scheiber and L. Romaner, Acta Mater. **221**, 117393 (2021).